Soft Matter

Metallic Microswimmers Driven up the Wall by Gravity

Journal:	*Soft Matter*
Manuscript ID	SM-ART-04-2021-000554.R1
Article Type:	Paper
Date Submitted by the Author:	24-May-2021
Complete List of Authors:	Brosseau, Quentin; University of Pennsylvania, Engineering Balboa Usabiaga, Florencio; Basque Center for Applied Mathematics, Lushi, Enkeleida; New Jersey Institute of Technology, Mathematical Sciences Wu, Yang; New York University, Chemistry Ristroph, Leif; New York University, Couant Institute of Mathematical Sciences Ward, Michael; New York University, Chemistry Shelley, Michael; New York University, Courant Institute Zhang, Jun; New York University, Courant Institute

Soft Matter

ARTICLE TYPE

Cite this: DOI: 00.0000/xxxxxxxxxx

Metallic Microswimmers Driven up the Wall by Gravity†

Quentin Brosseau[a,¶], Florencio Balboa Usabiaga[b,¶], Enkeleida Lushi[c], Yang Wu[d], Leif Ristroph[a], Michael D. Ward[d], Michael J. Shelley[a,b] and Jun Zhang[a,e,f]

Received Date
Accepted Date

DOI: 00.0000/xxxxxxxxxx

Experiments on autophoretic bimetallic nanorods propelling within a fuel of hydrogen peroxide show that tail-heavy swimmers preferentially orient upwards and ascend along inclined planes. We show that such gravitaxis is strongly facilitated by interactions with solid boundaries, allowing even ultraheavy microswimmers to climb nearly vertical surfaces. Theory and simulations show that the buoyancy or gravitational torque that tends to align the rods is reinforced by a fore-aft drag asymmetry induced by hydrodynamic interactions with the wall.

As part of their survival, many microorganisms, such as the algae *C. reinhardtii*, *E. gracilis*, or *Paramecia*, need to swim up against gravity. Such behavior is known as *gravitaxis*. These swimmers, when pulled by gravity, align vertically due to a fore-aft drag asymmetry along their bodies that generates a hydrodynamic torque.[1–6] Inhomogeneous density distributions within their bodies can also lead to buoyancy torques and vertical alignment.[7] Once oriented vertically their propulsion allows vertical migration. When in a group, these torques contribute to the emergence of colonial bioconvective patterns and to the stratification of swimmers in the bulk.[8–11] Near confining walls, the dynamics of any swimmer is expected to change due not only to gravity but also to hydrodynamic interactions with boundaries.[12,13] Indeed, many microbes inhabit wet soils and other porous media where sloped boundaries are omnipresent.[14,15] A natural question is whether such walls will suppress or enhance gravitaxis.

The design of artificial microswimmers can incorporate the working principles underlying organismal gravitaxis to drive, direct, and optimize the motion of self-propelled colloids.[16,17] For example, spherical polystyrene beads coated with a heavy metallic cap on its trailing pole and fueled by hydrogen peroxide swim up in the bulk.[18,19] Swimmer shape also affects trajectory, as demonstrated for L-shaped autophoretic colloids (powered by light) swimming on an inclined plane, wherein asymmetric propulsion-to-drag distribution allowed steady upslope movement plus curved motions and sedimentation.[20]

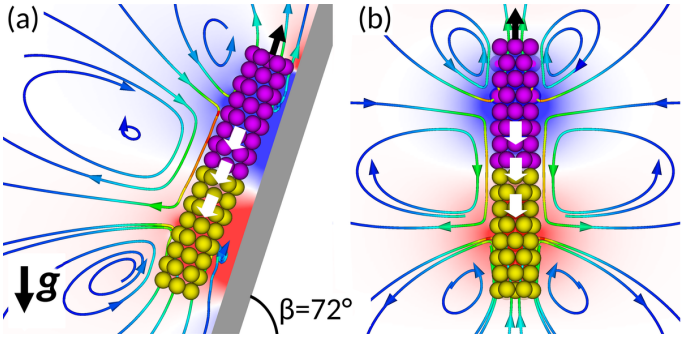

Fig. 1 Climbing rod and flow fields. Computed flow streamlines and regions of high/low (red/blue background) pressure from a simulation of a gold-rhodium rod climbing a steep wall: views from the side (a) and the front of the wall (b). In our model, the reduction and oxidation of H_2O_2 on the metallic segments generate an active slip layer (white arrows) near the bimetallic junction, propelling the rod. Notice that the rod has a dynamically determined head-down tilt with respect to the wall.

We describe the gravitactic behavior of active bimetallic rods, combining experiments, theory and simulations to demonstrate that these heavy nanomotors can swim up inclined walls, even very steep ones; see Fig. 1. Their behavior resembles some aspects of organismal gravitaxis, as these nanomotors are tail heavy such that density inhomogeneity contributes to an upright orientation of the rods. Direct real-time observation reveals that rods of homogeneous density sediment, i.e. do not climb, along the wall. Surprisingly, however, these rods are subject to a gravitactic bias that slows their sedimenting speeds. Our theoretical analysis and simulations demonstrate that the latter result can be explained by an effective fore-aft asymmetry in the hydrodynamic interaction between the rod and the nearby wall. This additional hydrodynamic effect enhances the gravitactic behavior of rods with density inhomogeneity.

[a] *Applied Mathematics Laboratory, Courant Institute, New York University, NY NY 10012, USA.*
[b] *Flatiron Institute, Simons Foundation, NY NY 10010, USA.*
[c] *Dept. of Math. Sciences, New Jersey Institute of Technology, Newark NJ 07102, USA.*
[d] *Dept. of Chemistry, New York University, NY NY 10012, USA.*
[e] *Dept. of Physics, New York University, NY NY 10003, USA.*
[f] *NYU-ECNU Physics and Mathematics Research Institutes, New York University Shanghai, Shanghai 200062, China.*
[¶] *These authors contributed equally to this work.*

† Electronic Supplementary Information (ESI) available: [details of any supplementary information available should be included here]. See DOI: 10.1039/cXsm00000x/

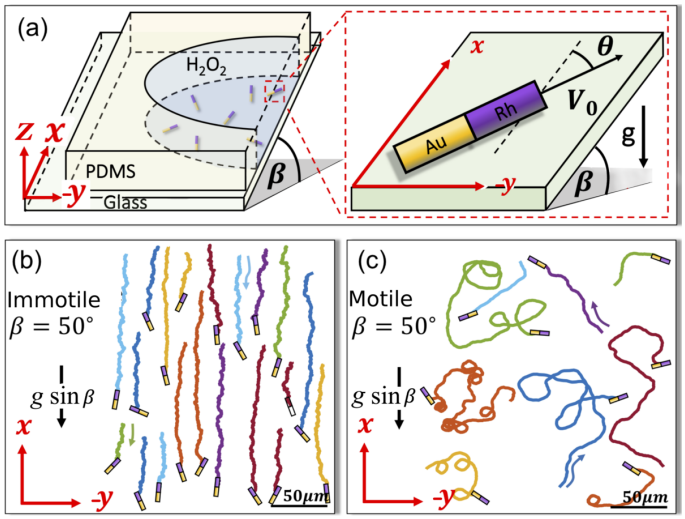

Fig. 2 Au-Rh bimetallic rods moving on an inclined wall. (a) Cutaway view of our experimental setup. The rods were enclosed in a chamber containing H_2O_2 solution. The inclination angle β is controlled by a super-structure encasing the chamber and optical microscope (not shown). (b) Trajectories acquired over 2 minutes of recording for Au-Rh rods on a surface inclined $50°$ for immotile rods (size exaggerated) when H_2O_2 is absent. (c) Motile rods (with 30% H_2O_2) were seen to make random but overall upward motion against gravity, an effect more evident from statistical analysis.

1 Experimental Setup and Results

The bimetallic swimmers used herein were $2.5\ \mu$m long gold-rhodium (Au-Rh) or $2.0\ \mu$m gold-platinum (Au-Pt) rods having diameter $d \approx 0.3\ \mu$m. The rods were synthesized by electrodeposition in anodized aluminum oxide templates according to a previously reported protocol.[21,22] The metallic segments were either length-symmetric (1:1) Au:Rh or Au:Pt rods, or length-asymmetric (3:1) Au:Pt with long-gold and short-platinum segments. More details on the rod synthesis is provided in the Supplementary Material.[23]

These rods self-propel when submersed in aqueous hydrogen peroxide (H_2O_2) solutions as fuel[24]. The fuel reduction/oxidation occurs on the Au/Pt or Au/Rh segments, creating an uneven charge distribution along the rod. The resulting electric field induces ionic migration in the rods' diffuse layer, creating a "slip layer" of fluid that envelops the rod and is likely most pronounced at the junction between the two metals[25]. This fluid displacement, due to momentum conservation, results in rod movement in the opposite direction, with the rhodium or platinum segment leading the motion.[26,27] The geometrically symmetric Au-Rh rods have a density asymmetry of ratio roughly 3:2 between the two segments, as $\rho_{\mathrm{Au}} = 19.32\,\mathrm{g/cm^3}$ and $\rho_{\mathrm{Rh}} = 12.41\,\mathrm{g/cm^3}$. Consequently, the rod Center of Mass (CoM) sits rearwards, resulting in a tail-heavy rod. In contrast, platinum is only slightly denser than gold, $\rho_{\mathrm{Pt}} = 21.45\,\mathrm{g/cm^3}$, such that the density of Au-Pt rods is nearly balanced. The fluid density is typically $\rho_{\mathrm{f}} \approx 1.1\,\mathrm{g/cm^3}$, depending on the amount of H_2O_2 added to water.

We used a Nikon Eclipse 80i microscope mounted on a custom-made tilting structure that permits adjustment to prescribed inclinations from horizontal to vertical (tilt angle $\beta \in [0°, 90°]$). The experimental chamber was mounted on the microscope's stage and positioned to ensure a fixed alignment with the optics. The chamber was a circular well with volume $\sim 1\,\mathrm{cm^3}$, cut from a $0.5\,\mathrm{cm}$ thick PDMS slab and mounted on a glass slide, as illustrated in Fig. 2a. This chamber was filled with H_2O_2 solution, followed by the addition of the bimetallic rods. The chamber was then capped with a coverslip to ensure an optically flat surface for observation and prevent fluid leakage.

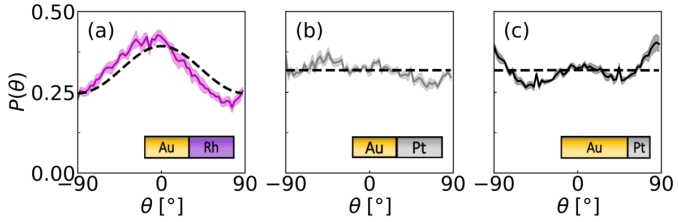

Fig. 3 Orientations of sedimenting immotile rods on inclined walls. Without H_2O_2, rods sediment, the distribution of their angles with the x-axis, $P(\theta)$, along a wall with inclination $\beta = 70°$ are shown for (a) Au-Rh tail-heavy rods and Au-Pt density-even rods (b)symmetric and (c) asymmetric with long-gold segment. Continuous lines with confidence interval (one std. error) experimental results; dashed lines fit to Eq. (6).

The kinematic characterization of the rods was done with the chamber positioned horizontally ($\beta = 0°$), as the rods sediment to the bottom and move about. Their movements in the focal plane of a 40X objective lens was recorded at a rate of $25\,$frames/s. Typically, the particle motion was measured for 2 minutes, such as the H_2O_2 concentration remained constant, and their trajectories analyzed using the `MatLab Image Processing Toolbox` and a custom-written software. The characteristic swimming speeds under various H_2O_2 concentrations (15%-30%) were typically from 3 to $8\,\mu\mathrm{m/s}$.[23]

1.1 Immotile Rods on an Inclined Wall

In the absence of H_2O_2, Au-Rh and Au-Pt rods were immotile. Since gravitational force dominates over thermal forces, the rods, unsurprisingly, slid down in rectilinear trajectories (Fig. 2b). The distribution of the angle between the rod axis and $\boldsymbol{x}$, $P(\theta)$, has a maximum at the vertical direction, $\theta = 0$, for tail-heavy Au-Rh rods (Fig. 3a) and is rather flat for both types of density-balanced Au-Pt rods (Fig. 3b, c). In the absence of reduction/oxidation reactions (propulsion) the orientation preference can only be linked to the density distribution of the rods. Here, the buoyancy (geometric) center of a Au-Rh rod differs from the CoM, giving rise to a torque that reorients the rod. The tail-heavy Au-Rh rods sediment with their gold ends leading and long-axis along the gravitational field.

1.2 Motile Rods

When submerged in an aqueous solution containing H_2O_2 fuel, the rods self-propel along the inclined wall, as illustrated in Fig. 2c. Their trajectories become highly nontrivial and exhibit movement up the wall against gravity as well as sideways and downward movements. Their gravitactic behavior is made more evident through statistical analysis of the trajectories. As illus-

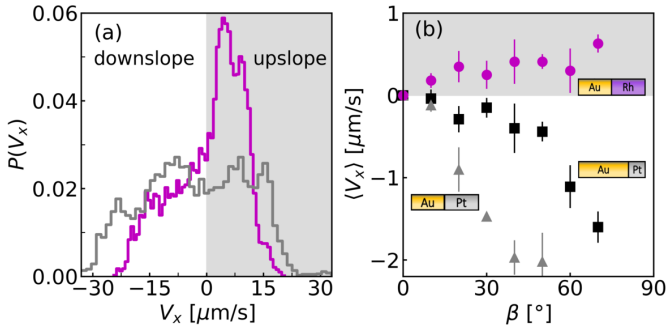

Fig. 4 Velocity of motile rods. (a) Velocity distribution of tail-heavy Au-Rh swimmers ▬ and symmetric density-balanced, 1:1 Au-Pt swimmers ▬ on a wall with inclination $\beta = 70°$. Overall, the Au-Rh rods swim upslope and perform gravitaxis while Au-Pt rods sediment. (b) The average velocity along the x-axis $\langle V_x \rangle$ vs. wall inclination β for three rod types with comparable swimming speed V_0: Au-Rh (●, $V_0 = 8.0 \pm 1.0\,\mu$m/s), symmetric Au-Pt (▲, $V_0 = 6.1 \pm 0.8\,\mu$m/s) and long-gold Au-Pt (■, , $V_0 = 6.5 \pm 0.7\,\mu$m/s). Au-Rh rods show increasing gravitactic ability with increased inclination, and Au-Pt rods sediment at different rates depending on their segmental ratios.

trated in Fig. 4a, the velocity distribution $P(V_x)$ at an inclination $\beta = 70°$ reveals that tail-heavy Au-Rh rods were biased towards upslope swimming. Density-balanced Au-Pt rods, however, display overall downward movement.

Fig. 4b depicts the mean velocity $\langle V_x \rangle$ for different wall inclinations, β, and for all three swimmer types. Tail-heavy Au-Rh rods clearly swim upslope. This tendency increases with β, whereas density-balanced Au-Pt rods sediment downslope. Notably, symmetric Au-Pt rods sediment faster downslope than asymmetric 3:1 long-gold Au-Pt rods at any inclination β. The slight gain in mass in the symmetric rod due to the longer Pt segment is not sufficient to explain its faster sedimentation. The next section addresses the role of hydrodynamic interactions between the rods and the wall in the gravitactic response and how it might control the sedimentation speed.

2 Modeling and Proving Gravitaxis

Two methods were used to model gravitaxis. The first is a full hydrodynamic description of the rods and the second is a simplified mechanical model. In the first method, each rod was modeled as a rigid body with an active slip layer centered in the bimetallic junction, see Fig. 1. The Stokes equations were solved to determine the surrounding flow and pressure fields in the presence of the wall, and consequently the rod orientation and swimming speed. The Stokes equations were solved with the Rigid Multiblob method.[23,28–31] In this method the rod surface is discretized by a set of N blobs with positions $(\boldsymbol{r}_i - \boldsymbol{q})$ relative to the rod tracking point $\boldsymbol{q}$. The slip condition, Eq. (1), and the balance of force and torque, Eq. (2), form a linear system that is solved for the rod linear and angular velocities, $\boldsymbol{u}$ and $\boldsymbol{\omega}$,

$$\sum_j^N \boldsymbol{M}_{ij}\boldsymbol{\lambda}_j = \boldsymbol{u} + \boldsymbol{\omega} \times (\boldsymbol{r}_i - \boldsymbol{q}) + \widetilde{\boldsymbol{u}}_i \quad \text{for } i = 1, \ldots, N, \tag{1}$$

$$\sum_i^N \boldsymbol{\lambda}_i = \boldsymbol{F}, \quad \sum_i^N (\boldsymbol{r}_i - \boldsymbol{q}) \times \boldsymbol{\lambda}_i = \boldsymbol{\tau}. \tag{2}$$

In the above linear system $\boldsymbol{\lambda}_i$ is the constraint force acting on the blobs to enforce a rigid motion and $\widetilde{\boldsymbol{u}}_i$ is the prescribed active slip on the blobs. The matrix $\boldsymbol{M}$ captures the hydrodynamic interaction between blobs, $\boldsymbol{M}_{ij}\boldsymbol{\lambda}_j$ being the flow generated at blob i by the constraint force acting on blob j. The matrix $\boldsymbol{M}$ is a regularization of the Green's function of the Stokes equation with the appropriate boundary conditions, i.e. no-slip at the wall.[32,33] We used the so-called Rotne-Prager approximation with wall corrections which has an analytical expression.[34] The external force and torque, $\boldsymbol{F}$ and $\boldsymbol{\tau}$, acting on the rod included the effect of gravity and the steric interactions with the wall.

In the experiments the active slip was created by the breakdown of H_2O_2 near the rod surface.[26,27] Numerical simulations of the full Stokes-electrochemical equations have shown that the charge gradients created by the fuel reduction/oxidation are larger near the bimetallic junction leading to a stronger slip in that sector.[25] In our numerical modeling instead of solving the complex reduction/oxidation reaction we assumed that a section of the rod surface was covered by an active slip of constant magnitude, $\widetilde{u}_s = 30\,\mu$m/s, parallel to the rod axis and centered near the metal-metal junction.[31] Additionally, since the rods worked as a battery with an active anode (Rh/Pt segment) and cathode (Au segment),[26] we assumed that the rate of the redox reaction was controlled by the smaller metal segment. Therefore, we made the length of the active section, L_s, proportional to the length of the smaller electrode

$$L_s = \begin{cases} 2L_{\text{Au}} & \text{if } L_{\text{Au}} \leq L/4, \\ L/2 & \text{if } L/4 \leq L_{\text{Au}} \leq 3L/4 \\ L - 2L_{\text{Au}} & \text{if } L_{\text{Au}} \geq 3L/4, \end{cases} \tag{3}$$

where L is the length of the rod and L_{Au} the length of the gold segment.

Our second model aims to understand the observed gravitaxis of Au-Rh swimmers and the controllable sedimentation (by different segmental ratios) of Au-Pt swimmers. The swimming rods were observed to remain close to the wall, previous reports have revealed that immotile rods remain parallel to the wall while motile rods swim with a head-down tilt angle α[31,35]; see Figs. 1 and 5a inset. The second model assumes that rod trajectories are two-dimensional, in the xy-plane parallel to the wall, and it describes the rod configuration by a tracking point (e.g. any fixed point on the rod) $\boldsymbol{x}(t) \in \mathbb{R}^2$ and the rod orientation $\theta(t)$ with respect to the x-axis. The rod is now a Brownian particle with swimming speed V_0, subject to a gravitational force $\boldsymbol{F}$ and torque

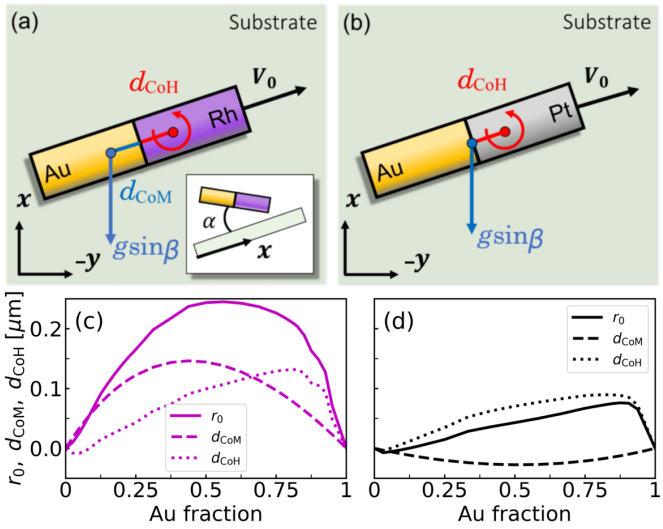

Fig. 5 Model for gravitaxis close to a wall. Body forces act on the rod's center of mass (CoM) whereas rotation occurs around the center of hydrodynamic stress (CoH). (a) Tail-heavy rods experience a gravitational torque since CoM sits rearward and CoH headward. (b) Density-balanced rods experience a torque due only to the shifted CoH from the center. (c, d) Values for d_{CoM} and d_{CoH}, the distances measured from the rod's center to the CoM and CoH, respectively, from full hydrodynamic simulations, for (c) Au-Rh and (d) Au-Pt rods with varying gold lengths. Negative values of d_{CoM} indicate a CoM displaced headward.

τ about the tracking point,

$$\begin{pmatrix} \dot{\boldsymbol{x}} \\ \dot{\theta} \end{pmatrix} = \begin{pmatrix} V_0\cos\theta \\ V_0\sin\theta \\ 0 \end{pmatrix} + \boldsymbol{M}\begin{pmatrix} \boldsymbol{F} \\ \tau \end{pmatrix} + \sqrt{2k_BT}\boldsymbol{M}^{1/2}\boldsymbol{W}. \tag{4}$$

The 3×3 mobility matrix $\boldsymbol{M}$, calculated at the tracking point, couples the force and torque to the linear and angular velocities while $\boldsymbol{W}\in\mathbb{R}^3$ is a white noise vector that generates the Brownian motion. The force, $\boldsymbol{F}=-mg\boldsymbol{e}_x\sin\beta$, is proportional to m the rod excess of mass over the displaced fluid, acceleration due to gravity g and increases with the wall inclination β. The gravitational reorienting torque τ (normal to the xy-plane) has magnitude $r_0 mg\sin\beta\cos\alpha\sin\theta$, where r_0 is the lever arm, i.e. the distance between the tracking point and the rod CoM.

Analyzing (4) is difficult because the rod translational and rotational dynamics are coupled. However, the orientation equation can be decoupled from the translation if the tracking point is chosen to be the center of rotation. The center of rotation is defined to be a pivot point about which an applied torque generates only rotation and not translation, whereas a net body force generates only translation and not rotation.[36–38] Such a pivot point is known to exist for two dimensional motion.[28] We denote this pivot point as the *Center of Hydrodynamic stress* (CoH). Using the CoH as the tracking point the orientation equation simplifies to

$$\frac{\mathrm{d}\theta}{\mathrm{d}t} = M_{\omega\tau}\tau + \sqrt{2k_BT}M_{\omega\tau}^{1/2}W_\theta. \tag{5}$$

For a rod in the bulk, far from any walls, the CoH is located at its geometric center. Near to a wall the CoH location may shift. For swimmers with a head-down tilt ($\alpha>0$) the increased resistance near the front displaces the CoH headward from their geometric centers.[23] Therefore, the lever arm at which a body force exerts a gravitational torque can be decomposed into two contributions, $r_0 = d_{CoM}+d_{CoH}$, i.e. distances measured from the rod's center to the CoM and CoH, respectively; see Figs. 5a, b. The larger the lever arm r_0, the larger the reorienting torque. This increased torque can dominate over the disorienting thermal fluctuations. Thus, once oriented upwards by the gravitational torque, a swimmer may move upwards gravitactically.

A sizable level arm r_0 can be achieved using metals with density contrast (e.g. in the Au-Rh case, the CoM sits rearwards). For the Au-Rh rods, d_{CoM} is maximized for approximately symmetric rods, i.e. $L_{Au}\approx L/2$, see Figs. 5c.

The d_{CoH} can be increased by moving the metal junction, and thus the location of the slip layer, headward. This fluid layer, which propels the rods, creates a pressure field that tilts the rods.[31] Such head-down tilt makes the leading portion of the rod closer to the solid wall than the trailing portion, see Fig. 1. The resulting resistance difference, higher near the head but lower at the tail, shifts the CoH headward and thus increases d_{CoH}. Therefore, the location of the junction largely determines the position of the CoH. Figs. 5c, d illustrate the values (dotted curves) of d_{CoH}, as functions of the position where two metals join, obtained with our full hydrodynamic model. Combining both contributions to the lever arm, r_0 (solid curves in Fig. 5c, d), the model predicts that the gravitactic effect for Au-Rh rods will be maximized for length-symmetric swimmers while for Au-Pt rods will be maximized for rods with long gold segments. This is consistent with our experimental results shown in Fig. 4; some of these predictions are further validated next.

2.1 Quantifying the Lever Arm

To test the coupled effects of gravity and hydrodynamic interactions with the wall, we examine the orientation of motile rods. The probability density function (PDF) of the angle θ can be calculated from Eq. (5).[19] The experiments measure the angle formed by the rod axis with the x-axis and do not distinguish the orientation θ from $\theta'=\theta-180°$. The PDF for the angle wrapped to $[-90°, 90°]$ is

$$P(\theta) = \frac{e^{K\cos\theta}+e^{-K\cos\theta}}{2\pi I_0(K)}, \tag{6}$$

where $I_0(K)$ is the modified Bessel function of order zero and $K=r_0 mg\sin\beta\cos\alpha/k_BT$ is the ratio between the gravitational torque and the thermal energy, which randomizes the rod orientation. As shown in the supplement, upward swimming is possible when K is larger than the ratio between the sedimentation velocity and the intrinsic swimming speed V_0.[23] The experimental results are depicted in Fig. 6a, b. The peaks at $\theta=0°$ for both Au-Rh and Au-Pt rods are consistent with a lever arm $d_{CoH}>0$ as predicted by the mechanical model.

From $P(\theta)$ we extracted the parameter K that best fits the experimental results using Eq. (6); the values of K versus the wall

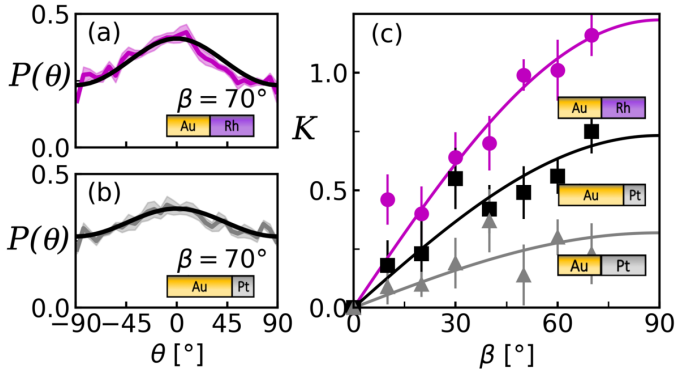

Fig. 6 Experiment vs. model. Experimental orientation distributions for motile (a) tail-heavy Au-Rh rods, and (b) asymmetric density-even Au-Pt rods, show peaks at $\theta = 0°$. Fitting the data by Eq. (6) (solid curves) we obtained K. (c) The extracted K values are plotted vs. tilt angle β. Values of r_0, further extracted by fitting K to the theoretical formula, $K \sim r_0 \sin\beta$ (solid lines), show gravitational torques act at lengths greater than d_{CoM} due to the shifted CoH in all 3 cases [tail-heavy (●), density balanced asymmetric (■) and density balanced symmetric rods (▲)].

inclination are shown in Fig. 6c. As expected from the model, K is proportional to $\sin\beta$. The results demonstrate that the overall torque is higher for Au-Rh rods, for which d_{CoM} is significant. The values of the lever arm r_0 can be extracted by fitting the values of K to the mechanical model prediction. For Au-Rh rods the fit yields $r_0 = 0.19\,\mu\mathrm{m}$, corresponding to $d_{\mathrm{CoH}} = 0.05\,\mu\mathrm{m}$, which is ahead of the rod's midpoint because its $d_{\mathrm{CoM}} = 0.14\,\mu\mathrm{m}$. Here, hydrodynamic effects account for about 25% of the torque felt by Au-Rh rods.

The Au-Pt rods were slightly head-heavy as platinum is denser than gold. In the cases of symmetric 1:1 Au:Pt and front-actuated 3:1 Au:Pt rods, d_{CoM} is -0.026 and -0.02 μm, respectively. This contribution is insufficient to produce a bias in the rod orientation. The experimental data suggest a torque larger than the one created by the density mismatch. A fit of the experimental results reveals that the distance of the CoH to the geometric center is larger for asymmetric rods ($d_{\mathrm{CoH}} = 0.14\,\mu\mathrm{m}$) than for the symmetric ones ($d_{\mathrm{CoH}} = 0.076\,\mu\mathrm{m}$). This arm length difference generates the distinct sedimentation speeds seen in our two Au-Pt rod types.

These values of K and d_{CoH} are larger than the ones obtained from Fig. 3 for immotile rods. For example, the values of d_{CoH} are 0.02, 0.03 and 0.03 for immotile Au-Rh, Au-Pt long gold and Au-Pt symmetric respectively. Clearly, the rods' activity modify their orientations.

3 Conclusions

Our results demonstrate gravitaxis using density unbalanced nanomotors fueled with H_2O_2. These "cliff climbers", which are about 15-20 times heavier than the surrounding fluid, move up steep walls. Interestingly, it is the gravitational pull that orients these tail-heavy rods and allows gravitaxis. Moreover, the emergent hydrodynamic effect when rods interact with the sloped walls[31,39] enhances the effect. Such enhancement can be used to control the sedimentation speed of falling rods and promote gravitaxis.

The microswimmer behavior reveals that an imbalance in density of the two metals results in a reorienting gravitational torque, due to the shift of its center of mass. Additionally, the shift of the center of rotation reveals the importance of the hydrodynamic interactions. Both effects take place and contribute to successful gravitaxis. In the synthetic world, the mechanisms studied in this work can be employed to design efficient gravitactors as well as microswimmers which gravitaxis is triggered near walls.

Acknowledgements

This work was supported primarily by the MRSEC Program of the National Science Foundation under Award DMR-1420073, and also by NSF Grants DMS-RTG-1646339, DMS-1463962 and DMS-1620331.

Conflicts of interest

There are no conflicts to declare.

Notes and references

1 A. M. Roberts, *Journal of Experimental Biology*, 1970, **53**, 687–699.
2 J. O. Kessler, *Nature*, 1985, **313**, 218.
3 A. M. Roberts and F. M. Deacon, *Journal of Fluid Mechanics*, 2002, **452**, 405–423.
4 A. M. Roberts, *Biological Bulletin*, 2006, **210**, 78–80.
5 A. M. Roberts, *Journal of Experimental Biology*, 2010, **213**, 4158–4162.
6 P. R. Richter, D.-P. Hader, R. J. Goncalves, M. A. Marcoval, V. E. Villafane and E. W. Helbling, *Photochemistry and Photobiology*, 2007, **83**, 810–817.
7 Y. Mogami, J. Ishii and S. A. Baba, *The Biological Bulletin*, 2001, **201**, 26–33.
8 S. Childress, M. Levandowsky and E. A. Spiegel, *Journal of Fluid Mechanics*, 1975, **69**, 591–613.
9 K. Wolff, A. M. Hahn and H. Stark, *The European Physical Journal E*, 2013, **36**, 43.
10 W. Yan and J. F. Brady, *Soft Matter*, 2015, **11**, 6235–6244.
11 F. Rühle and H. Stark, *arXiv preprint arXiv:2002.04323*, 2020.
12 F. Rühle, J. Blaschke, J.-T. Kuhr and H. Stark, *New Journal of Physics*, 2018, **20**, 025003.
13 S. Das, A. Garg, A. I. Campbell, J. Howse, A. Sen, D. Velegol, R. Golestanian and S. J. Ebbens, *Nat. Comm.*, 2015, **6**, 8999.
14 A. Petroff and A. Libchaber, *Proceedings of the National Academy of Sciences*, 2014, **111**, E537–E545.
15 A. P. Petroff, F. Tejera and A. Libchaber, *Journal of Statistical Physics*, 2017, **167**, 763–776.
16 D. P. Singh, W. E. Uspal, M. N. Popescu, L. G. Wilson and P. Fischer, *Advanced Functional Materials*, 2018, **28**, 1706660.
17 M. S. Rizvi, P. Peyla, A. Farutin and C. Misbah, *Phys. Rev. Fluids*, 2020, **5**, 033101.
18 J. Palacci, C. Cottin-Bizonne, C. Ybert and L. Bocquet, *Phys. Rev. Lett.*, 2010, **105**, 088304.

19 A. I. Campbell and S. J. Ebbens, *Langmuir*, 2013, **29**, 14066–14073.

20 B. ten Hagen, F. Kuemmel, R. Wittkowski, D. Takagi, H. Loewen and C. Bechinger, *Nature Communications*, 2014, **5**, 4829 EP.

21 W. F. Paxton, P. T. Baker, T. R. Kline, Y. Wang, T. E. Mallouk and A. Sen, *J. Am. Chem. Soc.*, 2006, **128**, 14881–14888.

22 M. J. Banholzer, L. Qin, J. E. Millstone, K. D. Osberg and C. A. Mirkin, *Nat. Prot.*, 2009, **4**, 838.

23 *Supplemental Material*, **URL to be inserted**, year.

24 Y. Wang, R. M. Hernandez, D. J. Bartlett, J. M. Bingham, T. R. Kline, A. Sen and T. E. Mallouk, *Langmuir*, 2006, **22**, 10451–10456.

25 J. L. Moran and J. D. Posner, *Physics of Fluids*, 2014, **26**, 042001.

26 J. L. Moran and J. D. Posner, *J. Fluid Mech.*, 2011, **680**, 31–66.

27 J. L. Moran and J. D. Posner, *Ann. Rev. Fluid Mech.*, 2017, **49**, 511–540.

28 S. Delong, F. Balboa Usabiaga and A. Donev, *J. Chem. Phys.*, 2015, **143**, 144107.

29 F. Balboa Usabiaga, B. Kallemov, B. Delmotte, A. P. S. Bhalla, B. E. Griffith and A. Donev, *Comm. App. Math. Comp. Sci.*, 2016, **11**, 217–296.

30 B. Sprinkle, F. Balboa Usabiaga, N. A. Patankar and A. Donev, *J. Chem. Phys.*, 2017, **147**, 244103.

31 Q. Brosseau, F. Balboa Usabiaga, E. Lushi, Y. Wu, L. Ristroph, J. Zhang, M. Ward and M. J. Shelley, *Phys. Rev. Lett.*, 2019, **123**, 178004.

32 J. Rotne and S. Prager, *J. Chem. Phys.*, 1969, **50**, 4831.

33 J. R. Blake, *Math. Proc. Cam. Phil. Soc.*, 1971, **70**, 303.

34 J. W. Swan and J. F. Brady, *Phys. Fluids*, 2007, **19**, 113306.

35 L. Ren, D. Zhou, Z. Mao, P. Xu, T. J. Huang and T. E. Mallouk, *ACS Nano*, 2017, **11**, 10591–10598.

36 J. Happel and H. Brenner, *Low Reynolds number hydrodynamics*, Springer Netherlands, 1983.

37 J. M. G. Bernal and J. G. De La Torre, *Biopolymers*, 1980, **19**, 751–766.

38 R. N. Georgiev, S. O. Toscano, W. E. Uspal, B. Bet, S. Samin, R. van Roij and H. B. Eral, *Proceedings of the National Academy of Sciences*, 2020, **117**, 21865–21872.

39 S. E. Spagnolie and E. Lauga, *J. Fluid Mech.*, 2012, **700**, 105–147.